Modelling of the ultrafast dynamics and surface plasmon properties of silicon upon irradiation with mid-IR femtosecond laser pulses

E. Petrakakis,[1,2] G. D. Tsibidis,[1,*] and E. Stratakis[1,3]

[1]*Institute of Electronic Structure and Laser (IESL), Foundation for Research and Technology (FORTH), N. Plastira 100, Vassilika Vouton, 70013 Heraklion, Crete, Greece*

[2]*Materials Science and Technology Department, University of Crete, 71003 Heraklion, Greece*

[3]*Department of Physics, University of Crete, 71003 Heraklion, Greece*

(Received 7 January 2019; revised manuscript received 24 April 2019; published 10 May 2019)

We present a theoretical investigation of the ultrafast processes and dynamics of the produced excited carriers upon irradiation of silicon with femtosecond pulsed lasers in the mid-infrared (mid-IR) spectral region. The evolution of the carrier density and thermal response of the electron-hole and lattice subsystems are analyzed for various wavelengths λ_L in the range between 2.2 and 3.3 μm, where the influence of two- and three-photon absorption mechanisms is explored. The role of induced Kerr effect is highlighted and it manifests a more pronounced influence at smaller wavelengths in the mid-IR range. Elaboration on the conditions that lead to surface plasmon (SP) excitation indicate the formation of weakly bound SP waves on the material surface. The lifetime of the excited SP is shown to rise upon increasing wavelength, yielding a larger one than that predicted for higher laser frequencies. The calculation of damage thresholds for various pulse durations τ_p shows that they rise according to a power law ($\sim \tau_p^{\zeta(\lambda_L)}$) where the increasing rate is determined by the exponent $\zeta(\lambda_L)$. Investigation of the multiphoton absorption rates and impact ionization contribution at different τ_p manifests a lower damage for $\lambda_L = 2.5\,\mu$m compared to that for $\lambda_L = 2.2\,\mu$m for long τ_p.

DOI: 10.1103/PhysRevB.99.195201

I. INTRODUCTION

Over the past decades, the use of ultrashort pulsed laser sources for material processing and associated laser-driven physical phenomena has received considerable attention due to the important technological applications, in particular in industry and medicine [1–10]. Various types of surface structures generated by laser pulses and, more specifically, the so-called laser-induced periodic surface structures (LIPSS) on solids have been studied extensively [11–25].

A key characteristic of the physical processes that account for the formation of LIPSS is that they were explored for laser pulses in a region between the visible and near-infrared spectrum ($\lambda_L < 1.5\,\mu$m) [26–31]. Nevertheless, to the best of our knowledge, laser machining in the mid-IR ($\lambda_L > 2\,\mu$m) is a rarely explored field [32,33]; the motivation to investigate the response of the irradiated semiconductor and relevant surface effects in the mid-IR region originates from the challenging opportunities in photonics for mid-IR radiation [34–39]. A fundamental question is whether the underlying physics that characterizes laser-matter interaction for mid-IR differs from that at lower spectral regions [40–46]. One characteristic example is that the proposed physical mechanism for the formation of subwavelength LIPSS (i.e., surface plasmon excitation-based mechanisms [15,30]) appears to behave differently if mid-IR sources are used [34]; for instance, the response of plasmons in the visible spectral region is largely dominated by (ohmic) losses in metals and the reaction time of the electrons. The former is closely related to the fact that the optical field of surface plasmons is weakly bound at mid-IR irradiation [34], unlike the confinement at visible wavelengths with direct implications in the energy absorption [47,48] and potential applications. Therefore, from both a fundamental and application point of view, it is important to explore the multiscale physical phenomena that take place for irradiation in the mid-IR regime.

To account for the influence of mid-IR photons on the physical processes, a number of critical factors should be considered: (i) the transparency of the material at larger λ_L [34], (ii) the significance of nonlinear processes such as Kerr effect or multiphoton absorption [35,36,49], (iii) the role of the wavelength in the modulation of the optical parameters, and (iv) the spatial and temporal width of an excited surface plasmon (SP) field in mid-IR. In this context, an interesting question that needs to be explored is whether SP excitation can be performed at substantially lower free-carrier densities or laser-beam energies.

The main focus of this study is to investigate the interaction of silicon (Si) with mid-IR femtosecond pulses, evaluate the variation of the optical properties of the material due to Kerr effect, quantify characteristics of the excited SP, and correlate irradiation conditions with surface damage. To this end, we present an extension of the well-established theoretical model that describes ultrafast dynamics in semiconductors, to account in this case for Si, for excitation and electron-phonon relaxation upon irradiation with ultrashort pulsed lasers in mid-IR in the range $2.2 \leqslant \lambda_L \leqslant 3.3\,\mu$m (Sec. II). A detailed analysis of the results that the theoretical model yields is presented in Sec. III by estimating the optical parameter varia-

*Corresponding author: tsibidis@iesl.forth.gr

tion, damage thresholds, and SP wave periodicities in various laser conditions. Furthermore, an analytical description of the spatial and temporal features of the SP waves excited with mid-IR pulses will be provided. Concluding remarks follow in Sec. IV.

II. THEORETICAL MODEL

A. Energy and particle balance equations

Following irradiation of Si with mid-IR femtosecond pulses in the range $2.2 \leqslant \lambda_L \leqslant 3.3\,\mu$m, it is assumed that two-photon and/or three-photon absorption mechanisms are sufficient to excite carriers from the valence to the conduction band, while higher-order photon processes are less likely to occur. The latter become important at even higher laser wavelengths; however, it is beyond the scope of the current work to include those laser frequencies. On the other hand, (linear) free-carrier photon absorption can increase the electron energy (but not the number of the excited carriers), while Auger recombination and impact ionization processes lead to decrease or increase of the carriers in the conduction band, respectively.

To describe the carrier excitation and relaxation processes, the relaxation-time approximation to Boltzmann's transport equation [15,30,40,50–52] is employed to determine the spatial ($\vec{r} = (x, y, z)$) and temporal dependence (t) of the carrier density number, carrier energy, and lattice energy. The carrier system is assumed to be nondegenerate (i.e., Maxell-Boltzmann distributed) as the adoption of a more rigorous approach is not expected to lead to substantial differences in the evaluation of the main observable effects (i.e., damage thresholds [51]). Based on this picture, the following set of coupled (nonlinear) energy and particle balance equations is used to derive the evolution of the carrier density number N_e, carrier temperature T_c, and lattice temperature T_L,

$$\begin{aligned} C_c\frac{\partial T_c}{\partial t} &= -\frac{C_c}{\tau_e}(T_c - T_L) + S(\vec{r},t),\\ C_L\frac{\partial T_L}{\partial t} &= \vec{\nabla}\bullet(K_L\vec{\nabla}T_L) + \frac{C_c}{\tau_e}(T_c - T_L),\\ \frac{\partial N_e}{\partial t} &= \frac{\beta_{\mathrm{TPA}}}{2\hbar\omega_L}I^2(\vec{r},t) + \frac{\gamma_{\mathrm{TPA}}}{3\hbar\omega_L}I^3(\vec{r},t)\\ &\quad - \gamma {N_e}^3 + \theta N_e - \vec{\nabla}\bullet\vec{J}, \end{aligned} \tag{1}$$

where C_c (C_L) is the carrier (lattice) heat capacity, k_e (k_h) are the heat conductivities of the electron (holes), $\hbar\omega_L$ stands for the photon energy, β_{TPA} and γ_{TPA} correspond to the two- and three-photon absorption coefficients, respectively, γ is the coefficient for Auger recombination, θ is the impact ionization coefficient, and τ_e is the carrier-phonon energy relaxation time. Other quantities that appear in Eq. (1) are the carrier current density $\vec{J}$, the heat current density $\vec{W}$, and S provided by the following expressions:

$$\begin{aligned} S(\vec{r},t) &= \alpha_{\mathrm{FCA}}I(\vec{r},t) + \beta_{\mathrm{TPA}}I^2(\vec{r},t) + \gamma_{\mathrm{TPA}}I^3(\vec{r},t) - \vec{\nabla}\bullet\vec{W}\\ &\quad - \frac{\partial N_e}{\partial t}(E_g + 3k_BT_e) - N_e\left(\frac{\partial E_g}{\partial T_L}\frac{\partial T_L}{\partial t} + \frac{\partial E_g}{\partial N_e}\frac{\partial N_e}{\partial t}\right),\\ \vec{W} &= (E_g + 4k_BT_e)\vec{J} - (k_e + k_h)\vec{\nabla}T_e,\\ \vec{J} &= -D\left(\vec{\nabla}N_e + \frac{N_e}{2k_BT_e}\vec{\nabla}E_g + \frac{N_e}{2T_e}\vec{\nabla}T_e\right), \end{aligned} \tag{2}$$

where α_{FCA} is the free-carrier absorption coefficient, D stands for the ambipolar carrier diffusivity, and k_B stands for the Boltzmann constant. Values of all parameters and coefficients used in this work are presented in Refs. [15,30,35,40,49–51,53–58] and Table I [59]. In previous studies, simulations manifested that although heat dissipation and particle transport are expected to increase the damage threshold predictions (results were given for $\lambda_L = 800$ nm and $\tau_p < 1$ ps [40,50,51]), neglecting these effects does not produce substantial changes to the material response. Nevertheless, in the current work, to perform a rigorous approach, the complete model was used although it is computationally more demanding (simulations details are described in Ref. [59]). This is due to the fact that energy dissipation away from the surface initially leads to a carrier decrease compared to when carrier transport is ignored. On the other hand, the transient energy gap (i.e., $\vec{\nabla}E_g$ in $\vec{J}$) has been shown to yield higher carrier densities at later times due to an effective carrier confinement [40,60]. In previous reports, it was shown that a precise investigation should include the influence of carrier confinement [60] and, therefore, in this study the roles of both carrier transport and transient energy gap are incorporated into the model to evaluate the interplay of the two mechanisms.

The energy flux $I(\vec{r},t)$ at a given thickness z inside the target [Eqs. (1) and (2)] is obtained by considering the laser energy propagation loss due to two-photon, three-photon, and free-carrier absorption, respectively [40],

$$\frac{\partial I(\vec{r},t)}{\partial z} = -\alpha_{\mathrm{FCA}}I(\vec{r},t) - \beta_{\mathrm{TPA}}I^2(\vec{r},t) - \gamma_{\mathrm{TPA}}I^3(\vec{r},t), \tag{3}$$

assuming that the laser beam is Gaussian both temporally and spatially, while the transmitted laser intensity at the incident surface is expressed in the following form:

$$\begin{aligned} I(\mathrm{x},\mathrm{y},\mathrm{z}=0,t) &= \frac{2\sqrt{\ln 2}E_p[1-\mathrm{R}(\mathrm{z}=0,\mathrm{t})]}{\sqrt{\pi}\tau_p}e^{-\left(\frac{2(x^2+y^2)}{R_0^2}\right)}\\ &\quad\times e^{-4\ln 2\left(\frac{t-t_0}{\tau_p}\right)^2}, \end{aligned} \tag{4}$$

where E_p is the fluence of the laser beam and τ_p is the pulse duration (i.e., full width at half maximum), R_0 is the irradiation spot-radius (distance from the center at which the intensity drops to $1/e^2$ of the maximum intensity), and R is the reflectivity while irradiation under normal incidence was assumed.

B. Optical properties of the irradiated material

The computation of the optical properties of the irradiated solid is derived from the dielectric constant of the material ε' [53],

$$\begin{aligned} \varepsilon' &= 1 + (\varepsilon_{un} - 1)\left(1 - \frac{N_e}{N_v}\right) - \frac{{e_c}^2N_e}{\varepsilon_0{\omega_L}^2}\frac{1}{\left(1 + i\frac{1}{\omega_L\tau_{\mathrm{col}}}\right)}\\ &\quad\times\left(\frac{1}{m^*_{e-\mathrm{cond}}} + \frac{1}{m^*_{h-\mathrm{cond}}}\right), \end{aligned} \tag{5}$$

where ε_{un} is the dielectric constant of the unexcited material at λ_L (for $\lambda_L \geqslant 2.5\,\mu$m [57] and for $\lambda_L \leqslant 2.5\,\mu$m [58]), e_c is the electron charge, $m^*_{e-\mathrm{cond}} = 0.26\,m_{e0}$ and $m^*_{h-\mathrm{cond}} = 0.37\,m_{e0}$

are the optical effective masses of the carriers [40,51] for conductivity calculations, m_{e0} is the electron mass, ε_0 is the permittivity of vacuum, N_v corresponds to the valence-band carrier density ($\sim 5 \times 10^{22}\,\mathrm{cm}^{-3}$), and τ_{col} stands for the carriers (electron-hole) collision time. In previous reports, more complex expressions were used [51] to compute τ_{col} through the inclusion of the influence of the electron-phonon, hole-phonon, and electron-hole collisions. More specifically, theoretical predictions showed that the choice of carrier collision frequency used in the Drude model strongly influences the calculated damage threshold. Nevertheless, in the current work, a constant value, $1/\tau_{\mathrm{col}} \sim 1.5 \times 10^{14}\,\mathrm{s}^{-1}$, is assumed as used in other works [15,30,61]; this choice of the collision frequency will be used to test the theoretical predictions against experimental observations in Sec. III.

The reflectivity and free-carrier absorption coefficients are given by the following expressions:

$$\alpha_{\mathrm{FCA}}(\mathrm{x},\mathrm{y},\mathrm{z},t) = \frac{2\omega_L k}{c},$$
$$R(\mathrm{x},\mathrm{y},\mathrm{z}=0,t) = \frac{(1-n)^2+k^2}{(1+n)^2+k^2}, \tag{6}$$

where c stands for the speed of light, while n and k [$n = n_0 + n_2 I$, $\varepsilon = (\mathrm{n}+\mathrm{ik})^2$] are the refractive index and extinction coefficient of the material, respectively [62],

$$\varepsilon = \varepsilon' + \Delta\varepsilon_{\mathrm{Kerr}},$$
$$\Delta\varepsilon_{\mathrm{Kerr}} = 2n_0 n_2 I + (n_2 I)^2, \tag{7}$$

while n_2 is the Kerr coefficient that corresponds to the nonlinear part of the refractive index due to the Kerr effect. It is related to the real part of the primary third-order susceptibility $\chi^{(3)'}$ through the following expression [49,63]:

$$n_2 = \frac{3}{4\varepsilon_0 c[n_0(\mathrm{N_e})]^2}\mathrm{Re}(\chi^{(3)'}), \tag{8}$$

while n_0 stands for the refractive index for $n_2 = 0$.

The computation of $\mathrm{Re}(\chi^{(3)'})$ is performed by following a fitting procedure on the averaged experimental data [49] in Refs. [35] and [54] [Fig. 1(a)], while Eqs. (5) and (8) indicate a carrier-density-dependent Kerr coefficient [Figs. 1(b) and 1(c)]. Results show significantly large values for the $\mathrm{Re}(\chi^{(3)'})$ and n_2 within the spectral region explored in this work ($2.2 \leqslant \lambda_L \leqslant 3.3\,\mu\mathrm{m}$), especially for low [Fig. 1(b)] and high [Fig. 1(c)] carrier density and, therefore, it is important to explore the role of the nonlinear part of the refractive index in the optical and thermal response of the material.

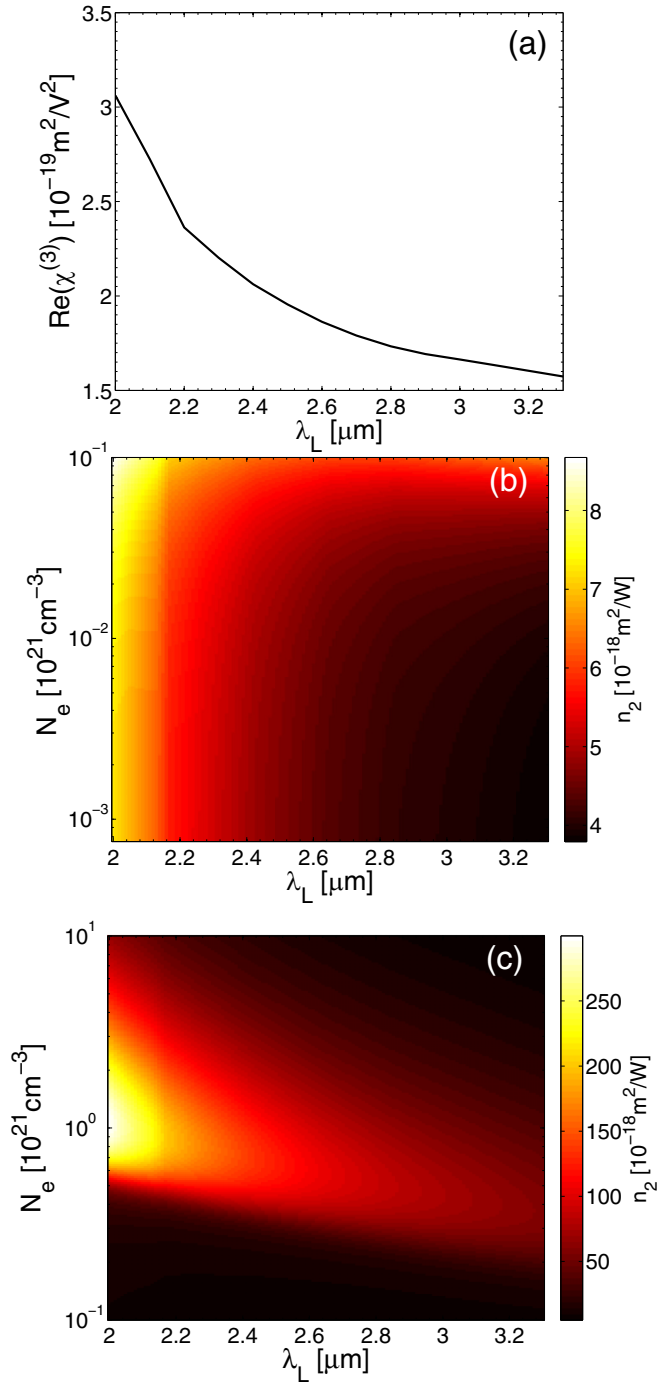

FIG. 1. (a) Computation of $\mathrm{Re}(\chi^{(3)'})$ as a function of the wavelength [35,49,54]. The dependence of the Kerr coefficient on λ_L and N_e is illustrated for (b) low and (c) high carrier densities.

III. RESULTS AND DISCUSSION

A. Impact of Kerr effect on ultrafast dynamics

The ultrafast dynamics and the thermal response of the heated material is investigated at three representative laser wavelengths λ_L (2.2, 2.5, and 3.3 μm) for $\tau_p = 100$ fs for (peak fluence) $E_p = 100\,\mathrm{mJ/cm}^2$. The selection of the wavelengths was based on the excitation properties at these wavelengths; more specifically, $\beta_{\mathrm{TPA}} \neq 0$ at 2.2 μm, while three-photon absorption dominates the carrier excitation at 2.5 and 3.3 μm. Based on the fact that the influence of the Kerr effect is more pronounced at lower laser wavelengths (Fig. 1), the range of laser frequencies for which the nonlinear part of the refractive index becomes significant should be highlighted [49]. It is evident that as the laser wavelength decreases, the impact of the Kerr effect is also expected to affect the ultrafast dynamics and thermal response. First, the nonlinearity of the material's refractive index leads to a variation of the absorbed energy and the temporal evolution of the reflectivity [Figs. 2(a) and 2(b), for $\lambda_L = 2.2\,\mu$m]. This variation is more pronounced at smaller wavelengths [Fig. 2(c)], while at larger

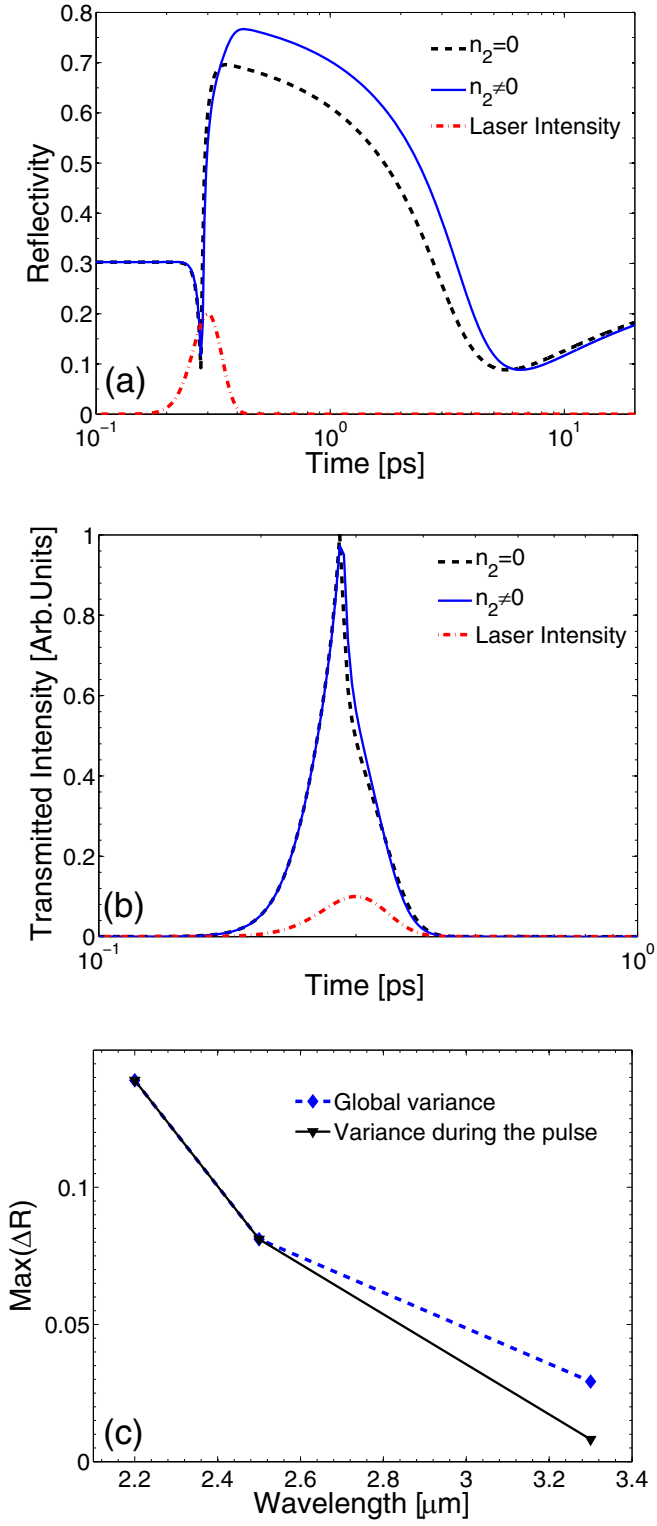

FIG. 2. (a) Dependence of reflectivity on the Kerr effect. The laser intensity is sketched in arbitrary units ($\lambda_L = 2.2\,\mu$m). (b) Effect of the Kerr effect on the intensity transmitted through the surface ($\lambda_L = 2.2\,\mu$m) (normalized to 1). (c) Maximum change of reflectivity (for $n_2 = 0$ and $n_2 \neq 0$) as a function of the wavelength. The solid line corresponds to variance of max(ΔR) in the whole range of timepoints, while the dashed line represent max(ΔR) up to the timepoint where the laser intensity is maximum ($E_p = 0.1\,\mathrm{J/cm^2}$ and $\tau_p = 100\,$fs, at $x = y = z = 0$).

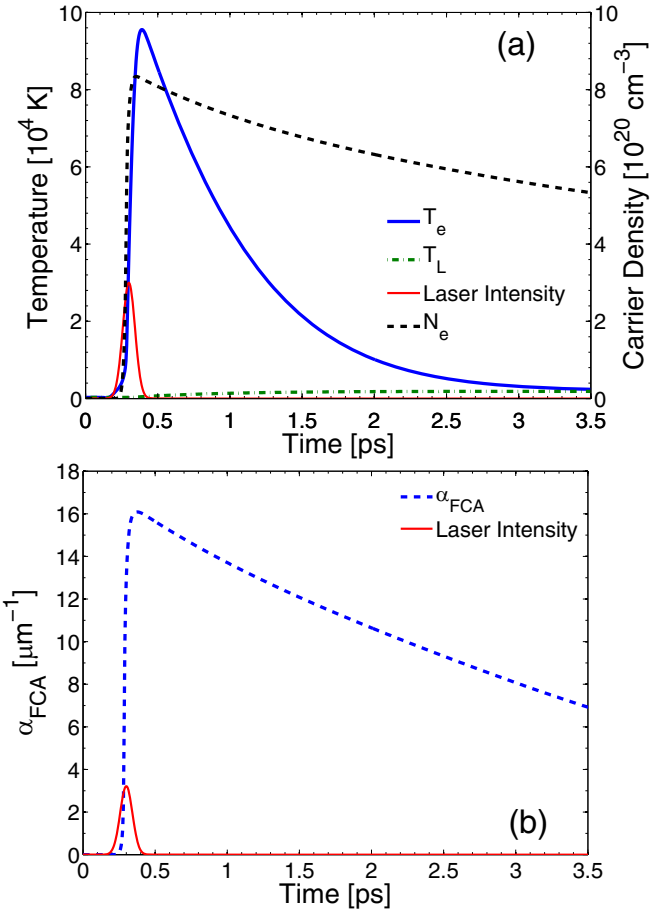

FIG. 3. (a) Evolution of T_e, T_L, N_e for $n_2 \neq 0$ (at $x = y = z = 0$). (b) Absorption coefficient evolution. The laser intensity in both graphs is sketched in arbitrary units ($E_p = 0.1\,\mathrm{J/cm^2}$, $\tau_p = 100\,$fs, $\lambda_L = 2.2\,\mu$m).

wavelengths in the mid-IR region ($\leqslant 3.3\,\mu$m), the Kerr effect is weaker and therefore it does not substantially affect the energy absorption. This behavior is illustrated both for small (up to the moment when the laser intensity is maximum) and for larger time ranges. It is noted that the reflectivity initially decreases during the pulse duration as the carrier density increases; then, its value ascends rapidly before the end of the pulse, followed by a fast decrease and a final slow increase to the initial value [Fig. 2(a)]. Similar evolution has been reported for lower wavelengths [29,40,53].

The evolution of the carrier density and the carrier and lattice temperatures are illustrated in Fig. 3(a). The maximum of T_e and N_e occurs shortly after the peak of the pulse. Interestingly, at low intensities (near the left tail of the Gaussian pulse), the carrier temperature does not exhibit a similar behavior to that demonstrated for silicon or other semiconductors (i.e., "a clamped region," which is represented by an initial increase followed by first a slight rise and then a sharp increase) [15,29,40,50,51]. This is due to the fact that the initial rise is attributed first to a single-photon absorption (which is absent for laser-beam frequencies in the mid-IR range) and second to a free-carrier absorption which, for low intensities, is zero for excitation with mid-IR pulses at

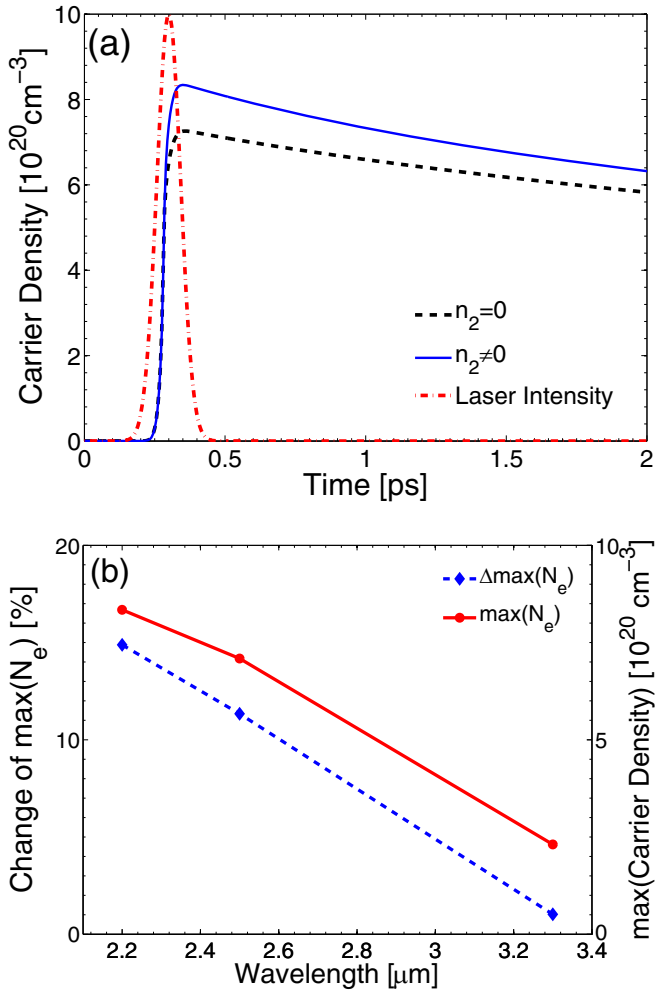

FIG. 4. (a) Dependence of evolution of N_e on the Kerr effect. The laser intensity is sketched in arbitrary units ($\lambda_L = 2.2\,\mu$m). (b) Percentage of change of max(N_e) (for $n_2 = 0$ and $n_2 \neq 0$) as a function of the wavelength. The maximum N_e is also illustrated ($E_p = 0.1\,\text{J/cm}^2$ and $\tau_p = 100\,\text{fs}$ at $x = y = z = 0$).

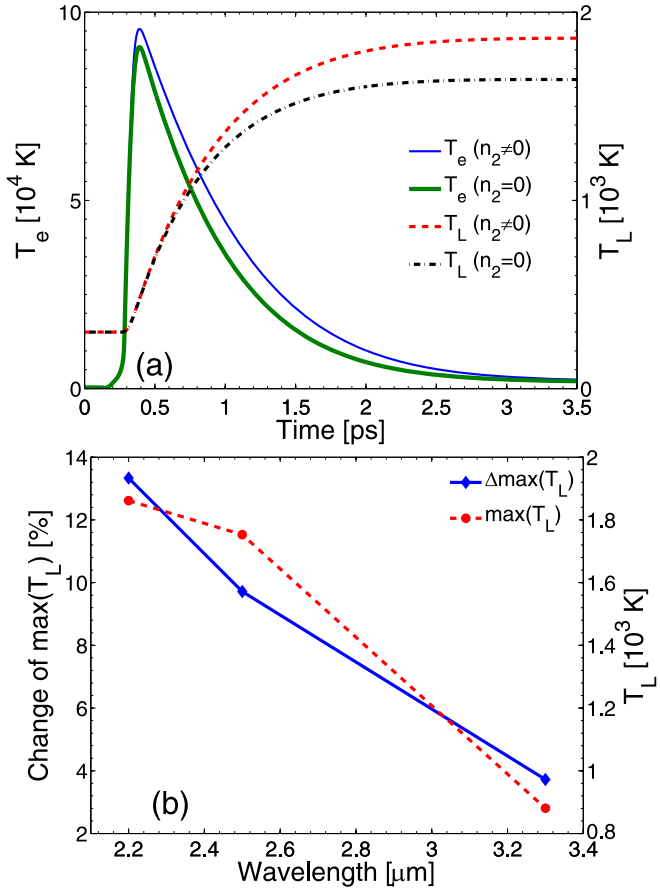

FIG. 5. (a) Dependence of evolution T_e and T_L on the Kerr effect. (b) Percentage change of max(T_L) (for $n_2 = 0$ and $n_2 \neq 0$) as a function of the wavelength ($E_p = 0.1\,\text{J/cm}^2$, $\lambda_L = 2.2\,\mu$m, and $\tau_p = 100\,\text{fs}$ at $x = y = z = 0$).

small timepoints. In regard to the latter, Fig. 3(b) illustrates that α_{FCA} gradually increases to nonzero values during the pulse duration, yielding a penetration depth which drops to $\sim 62.5\,\text{nm}$ when the laser is turned off. The rise of α_{FCA} due to the increase of the excited carrier density is expected to influence the amount of the absorbed energy. On the other hand, the relatively large free-carrier absorption at the end of the pulse combined with the large absorption depth through direct (two- and three-photon) absorption mechanisms suggest that there is not sufficient time for the carrier and heat transport terms to substantially change the carrier distribution that has been produced. Hence, neglecting the diffusion terms in Eqs. (1) and (2) is not expected to yield different overall behavior of the thermal response of the irradiated material.

Simulations results show that the Kerr effect always leads to larger (maximum) values of N_e [Fig. 4(a)]. It is evident that due to the variable absorption levels at different wavelengths, the induced density of the excited carriers is larger if the nonlinearities due to the Kerr effect are included in the model [Fig. 4(a)]. As expected, at larger wavelengths, the Kerr effect impact on the carrier density evolution is insignificant [Fig. 4(b)] due to the negligent influence of Kerr nonlinearities. It is noted that while the carrier dynamics analysis for smaller wavelengths ($\lambda_L = 2.2\,\mu$m) yields a maximum N_e larger by about 17% than the value obtained if the Kerr effect is ignored, the discrepancy is rather insignificant for larger wavelengths ($\lambda_L = 3.3\,\mu$m). The decrease of the maximum value of the carrier density with increasing λ_L is due to the impact of the ionization processes: at $\lambda_L = 2.2\,\mu$m, there is a dominant two-photon absorption-assisted ionization, while at larger wavelengths, $\beta_{\text{TPA}} = 0$ (for $\lambda_L = 2.5\,\mu$m) which enhances the impact of the three-photon absorption. At even larger wavelengths ($\lambda_L = 3.3\,\mu$m), the main ionization mechanism, the three-photon-assisted ionization process becomes very small due to the decrease of γ_{TPA} as λ_L increases [55]. Similar discrepancies to the one shown above as a result of the Kerr effect also occur for the electron and lattice temperatures. Figure 5(a) shows the rise of the lattice temperature that is demonstrated for $n_2 \neq 0$. It is evident that the Kerr effect causes a significantly enhanced thermal response of the material, which is reflected by the increased lattice temperature ($\sim 200\,\text{K}$ for $E_p = 100\,\text{mJ/cm}^2$ at $\lambda_L = 2.2\,\mu$m, while similar conclusions can also be drawn for different conditions). This behavior is of paramount importance as it is expected to

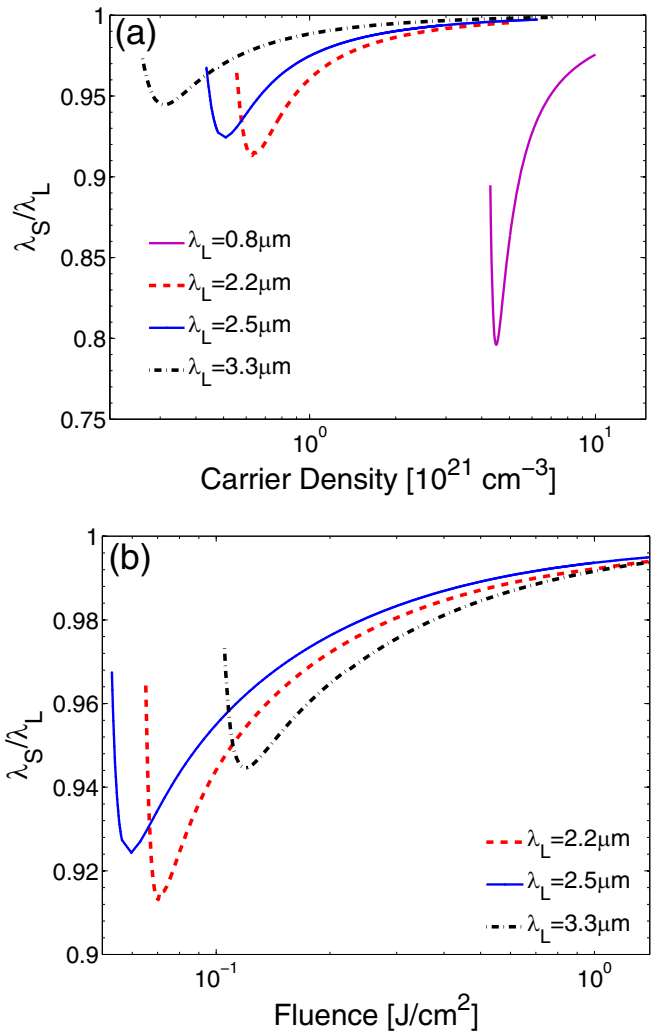

FIG. 6. Surface plasmon periodicity as a function of the (a) carrier density and (b) fluence at different wavelengths. ($\tau_p = 100$ fs).

influence the damage threshold values. To evaluate the impact of the laser wavelength, it turns out that the Kerr effect does not induce any meaningful change of the maximum lattice temperature at longer wavelengths [Fig. 5(b)]. Furthermore, the effect on the equilibration time or the evolution of T_e [Fig. 5(a)] appears to be insignificant.

B. Surface plasmon excitation

The condition $\mathrm{Re}(\varepsilon) < -1$ [59] and the solution of Eqs. (1)–(8) yield the value of the SP wavelength as a function of the carrier densities and the fluence (Fig. 6) for $\tau_p = 100$ fs for $\lambda_L = 2.2$, 2.5, and 3.3 μm. According to the theoretical predictions [Fig. 6(a)], a larger (maximum value of) carrier density is required to initiate SP excitation [at $\mathrm{Re}(\varepsilon) < -1$] as the laser wavelength decreases. On the other hand, an increase of the laser wavelength leads to smaller overall expected variation of the SP periodicity. More specifically, a comparison with results for larger laser frequencies ($\lambda_L = 800$ nm) manifests that for $\lambda_L = 2.2$, 2.5, and 3.3 μm, an average maximum drop of the λ_S yields values $\sim 0.91\,\lambda_L$ which is higher than the estimate for $\lambda_L = 800$ nm ($\sim 0.78\,\lambda_L$). Based on the results illustrated in Fig. 6, a large deviation of the ripple frequency is not expected for irradiation in the mid-IR spectral region, unlike predictions for $\lambda_L = 800$ nm. Furthermore, given the impact of the absorbed energy on the production of excited carriers, the SP periodicity was also calculated as a function of the fluence [Fig. 6(b)]. While at $\lambda_L = 3.3\,\mu$m, a larger peak fluence is necessary to excite SP, for $\lambda_L = 2.5\,\mu$m, a smaller fluence is required compared to that for $\lambda_L = 2.2\,\mu$m.

As excitation of surface plasmons and their interference with the incident beam is regarded as the predominant mechanism of periodic structure formation [15,30], the range of the computed SP wavelengths can provide an estimate of the expected subwavelength structures on the irradiated material for different N_e. More specifically, results illustrated in Fig. 6 indicate that subwavelength structures can be produced at substantially lower carrier densities and fluences than those required for pulses of periodicity equal to 800 nm. The above investigation and significant differences of the SP periodicities produced with mid-IR and lower wavelength are expected to provide the theoretical basis in future simulations of LIPSS formation mechanisms with mid-IR pulses [33,64]. Although a more systematic analysis of the periodic structure characteristics is required in the mid-IR spectral region, one interesting prospect of the employment of such pulses is the production (through coupling of the incident beam with the SP [15]) of larger than 2 μm periodicity LIPSS with orientation *perpendicular* to the polarization of the laser by using a small energy dose. By contrast, LIPSS with periodicity of this size (i.e., suprawavelength structures which are called grooves [24]) with $\lambda_L = 800$ nm are produced with orientation *parallel* to the polarization of the laser with relatively higher energy dose.

Apart from the SP wavelength, it is also important to compare other spatial features of these surface waves, such as their damping length, for their propagation along the surface, decay of the SP away from the surface, as well as their lifetime. More specifically,

(i) the range of values of the distance which the SP propagates along the surface is computed by the expression $\mathrm{L} = [2\mathrm{Im}(\sqrt{(\frac{\varepsilon\varepsilon_\mathrm{d}}{\varepsilon+\varepsilon_\mathrm{d}})})]^{-1}$ [48]. While for $\lambda_L = 800$ nm, L ranges from 0.130 to 25 μm, substantially larger values (one order of magnitude) between 0.830 and 193 μm, 1 and 340 μm, and 2 and 740 μm are predicted for $\lambda_L = 2.2$, 2.5, and 3.3 μm, respectively [Fig. 7(a)].

(ii) On the other hand, the decay of the SP away from the surface of the material is given by

$$\mathrm{L}_D = \frac{\lambda_L}{2\pi\,\mathrm{Im}\left(\sqrt{\frac{\varepsilon^2}{\varepsilon_d+\varepsilon}}\right)}, \tag{9}$$

for the $1/e$ decay of the electric field, assuming continuity of the electromagnetic field on the surface [65]. Results illustrated in Fig. 7(b) indicate a weak confinement of SP for wavelengths in the mid-IR region compared to the calculations for $\lambda_L = 800$ nm. It is evident that for carrier densities small enough but sufficiently high to initiate SP excitation, the decay length of the SP electric field inside the material is larger than 220 nm, which is three times the estimate for excitation with $\lambda_L = 800$ nm. The increasing monotonicity of

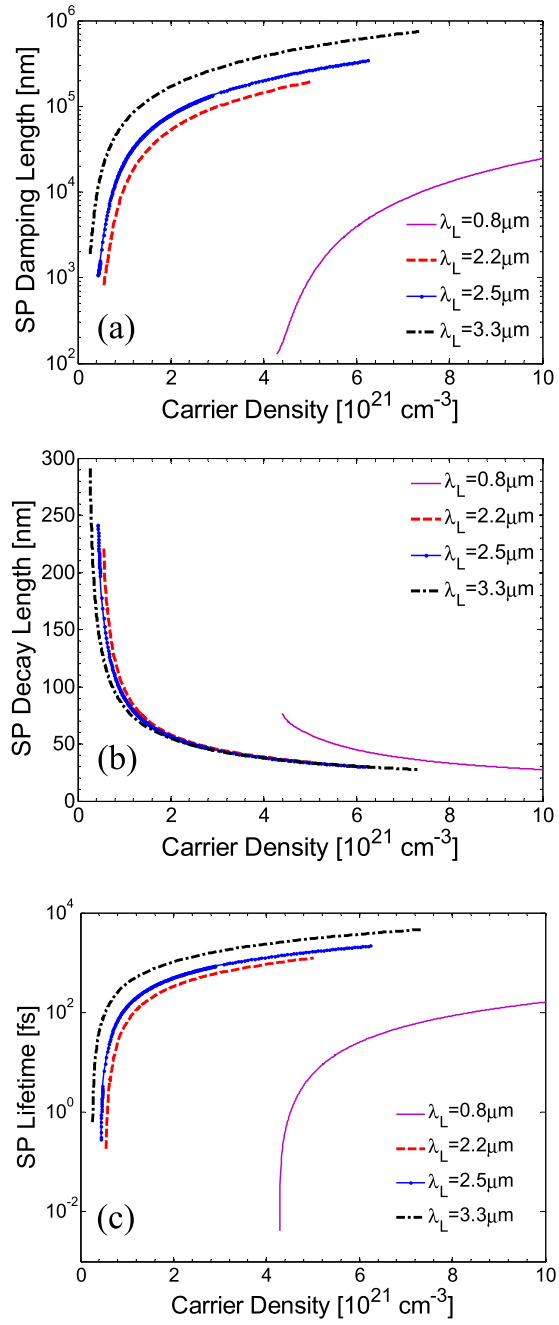

FIG. 7. Surface plasmon's (a) damping length, (b) decay length, and (c) lifetime at different laser wavelengths ($\tau_p = 100$ fs).

the L at larger wavelengths manifests that the confinement can be further weakened by using even larger laser wavelengths. By contrast, it is noted that at higher excitation levels in which larger carrier densities are produced, L_D values are comparable regardless of the light frequency used. The above results demonstrate quantitatively the weak confinement of SP on the material surface for mid-IR pulses compared to visible wavelengths [34]; furthermore, the correlation of the weakly bound SP with the excited carrier density can provide significant details of the laser conditions (i.e., fluence, pulse duration, and pulse wavelength) required to modulate the confinement.

(iii) Finally, the lifetime of the SP is calculated by the expression [47]

$$\tau_{\mathrm{SP}} = \frac{1}{2\mathrm{A}}$$

$$\mathrm{A} = \frac{\mathrm{c}}{2}\frac{2\pi}{\lambda_L}\frac{\mathrm{Re}\sqrt{\left(\frac{\varepsilon\varepsilon_d}{\varepsilon+\varepsilon_d}\right)}\mathrm{Im}(\varepsilon)}{\mathrm{Re}(\varepsilon)}\frac{\mathrm{Re}(\varepsilon_d)}{\mathrm{Re}(\varepsilon)+\mathrm{Re}(\varepsilon_d)}. \quad (10)$$

Results in Fig. 7(c) illustrate that there is an increase in the SP lifetime if mid-IR frequencies are used compared to predictions for $\lambda_L = 800$ nm. Interestingly, τ_{SP} is between one to two orders of magnitude larger for $\lambda_L = 2.2$, 2.5, and 3.3 μm. More specifically, the τ_{SP} range extends to some picoseconds for mid-IR, unlike for $\lambda_L = 800$ nm for which the SP lifetime lasts up to some hundreds of femtoseconds at large N_e. A similar increase in the SP lifetime for longer wavelengths has been reported in previous works for metals [47]. Given the significance of the lifetime of SP for the interference of the incident beam with surface plasmons [15,29,42], an increase of τ_{SP} appears to allow longer pulse temporal separation in the double-pulse laser-assisting technique to modify the surface profile of a material [26].

C. Damage threshold

One important parameter, both from fundamental and applied points of view, is the determination of the material damage threshold E_{DT}. In principle, there is an ambiguity of the definition of the damage threshold on whether mass removal is involved or, simply, a mass redistribution (i.e., due to melting and fluid transport) occurs. In the current work, the investigation focuses on the laser conditions that produce effects that raise the temperature of the lattice above the melting point but material volume does not vary. Therefore, E_{DT} is defined as the minimum fluence required to melt the material ($T_L > T_{\mathrm{melt}}$).

The dependence of E_{DT} as a function of the pulse duration and wavelength is illustrated in Fig. 8(a). It is noted that a pulse-duration increase leads to a decrease of the absorbed energy, which is also reflected on the reduced number of excitation carriers as shown in the Supplemental Material [59]. This behavior indicates that more energy is required to melt the material (i.e., E_{DT} increases). Simulation results show that the damage threshold varies as $\sim \tau_p^{\zeta(\lambda_L)}$ for pulse durations in the range [0.2 ps, 10 ps], where $\zeta(\lambda_L) \sim 0.552$, 0.562, 0.553 for $\lambda_L = 2.2$, 2.5, 3.3 μm, respectively. Similar power-law dependencies have been deduced for silicon and other materials after irradiation at lower wavelengths [50,66–69]. On the other hand, it is noted that [inset in Fig. 8(a)] for $\tau_p <$ 200 fs, there is a deviation from the aforementioned power-law dependency due to the influence of other characteristic times in the heating process such as the recombination and relaxation times. This behavior is more enhanced at lower wavelengths, $\lambda_L = 2.2$ and $\lambda_L = 2.5$ μm.

To elaborate further on the dependence of E_{DT} on the laser wavelength, it is important to examine this correlation with respect to the strength of the multiphoton excitation mechanisms as well as the factors that are capable to increase carrier excitation (i.e., impact ionization). More specifically, two distinct cases were analyzed: (i) $\beta_{\mathrm{TPA}} = 0.25$ cm/GW, $\gamma_{\mathrm{TPA}} =$

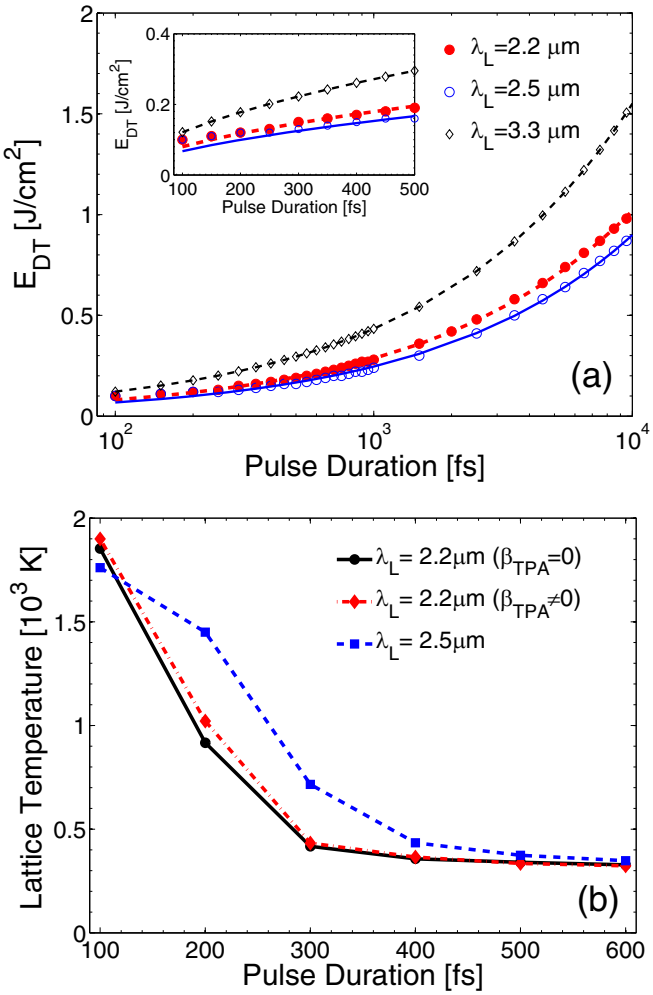

FIG. 8. (a) Damage threshold fluences E_{DT} vs pulse duration. The inset shows an enhanced view of E_{DT} for τ_p in the range [100 fs, 500 fs] (points represent the simulated data values, while lines are derived after fitting using a power law $\tau_p^{\zeta(\lambda_L)}$, i.e., thick dashed line for $\lambda_L = 2.2\,\mu$m, solid line for $\lambda_L = 2.5\,\mu$m, and thin dashed line for $\lambda_L = 3.3\,\mu$m). (b) Lattice temperature for two- and three-photon absorption for $\lambda_L = 2.2\,\mu$m and $\lambda_L = 2.5\,\mu$m at $E_p = 0.1\,\mathrm{J/cm^2}$ ($x = y = z = 0$).

$0.020\,\mathrm{cm^3/GW^2}$ (for $\lambda_L = 2.2\,\mu$m), (ii) $\beta_{\mathrm{TPA}} = 0\,\mathrm{cm/GW}$, $\gamma_{\mathrm{TPA}} = 0.0276\,\mathrm{cm^3/GW^2}$ (for $\lambda_L = 2.5\,\mu$m), and (iii)$\beta_{\mathrm{TPA}} = 0\,\mathrm{cm/GW}$, $\gamma_{\mathrm{TPA}} = 0.0017\,\mathrm{cm^3/GW^2}$ (for $\lambda_L = 3.3\,\mu$m) (Table I [55,59]). Interestingly, previous reports on silicon showed that for near-infrared pulses, avalanche (impact) ionization processes are the driving force for surface damage, which leads to a lower damage threshold for longer wavelengths [40]; that behavior could not be explained if one-photon absorption mechanisms accounted for the damage [70]. To investigate whether similar arguments hold for irradiation with pulses in the mid-IR range, simulations have also been carried out [59]. Results provide a compelling proof that impact ionization itself is sufficient to explain the initially surprising results that radiation with $\lambda_L = 2.5\,\mu$m requires less fluence to damage the material than laser sources of $\lambda_L = 2.2\,\mu$m; in contrast, for irradiation with beams of $\lambda_L = 3.3\,\mu$m in which a three-photon absorption mechanism dominates, melting of the material occurs at higher fluences. The effect of impact ionization contribution to the (maximum) carrier change rate [quantity θN_e in Eq. (1)] is illustrated as a function of the laser wavelength and the pulse duration for the damage threshold fluences. Thus, simulation results manifest in a conclusive way that the level of carrier density excitation due to, predominantly, impact ionization produces different behavior for the three wavelengths at higher τ_p; this justifies the aforementioned argument that avalanche effects do contribute to higher damage thresholds for $\lambda_L = 2.2\,\mu$m than for $\lambda_L = 2.5\,\mu$m. To further explain the damage threshold curves for $\lambda_L = 2.2$ and $\lambda_L = 2.5\,\mu$m, one also has to look at the absorption rates for the two- and three-photon absorption mechanisms as well as the strength of γ_{TPA}. To estimate the contribution of the two- and three-photon absorption in the produced excited carrier distribution, simulations have been performed for $E_p = 0.1\,\mathrm{J/cm^2}$ for six different pulse durations (in the range $\tau_p = 0.1$ to 0.6 ps) for $\lambda_L = 2.2$ and $\lambda_L = 2.5\,\mu$m. Results in Fig. 8(b) illustrate the maximum T_L where simulations for the complete model ($\beta_{\mathrm{TPA}} = 0.25\,\mathrm{cm/GW}$, $\gamma_{\mathrm{TPA}} = 0.020\,\mathrm{cm^3/GW^2}$) are shown for $\lambda_L = 2.2\,\mu$m, and it is compared with $\beta_{\mathrm{TPA}} = 0\,\mathrm{cm/GW}$, $\gamma_{\mathrm{TPA}} = 0.020\,\mathrm{cm^3/GW^2}$. All cases are tested against theoretical results for $\lambda_L = 2.5\,\mu$m ($\beta_{\mathrm{TPA}} = 0\,\mathrm{cm/GW}$, $\gamma_{\mathrm{TPA}} = 0.0276\,\mathrm{cm^3/GW^2}$). It is evident that for irradiation with $\lambda_L = 2.2\,\mu$m, the two-photon absorption does not influence the maximum lattice temperature for $\tau_p > 300$ fs (for $E_p = 0.1\,\mathrm{J/cm^2}$) and three-photon absorption dominates the excitation from the valence to the conduction band; in contrast, it appears that the significance of the two-photon absorption rate is more enhanced at decreasing pulse duration. Similar conclusions can be reached if higher intensities can be achieved by increasing the fluence. More specifically, at higher fluences, two-photon processes play a more important role, which is also projected on the produced enhanced lattice temperature with respect to the one for $\beta_{\mathrm{TPA}} = 0\,\mathrm{cm/GW}$, $\gamma_{\mathrm{TPA}} = 0.0276\,\mathrm{cm^3/GW^2}$ for $\lambda_L = 2.5\,\mu$m. On the other hand, as the pulse duration increases and exceeds $\tau_p = 300$ fs, the (almost minimum) influence of the two-photon absorption processes yields excitation predominantly through a three-photon absorption with $\gamma_{\mathrm{TPA}} = 0.020\,\mathrm{cm^3/GW^2}$; as this value gives a smaller three-photon absorption rate for $\lambda_L = 2.5\,\mu$m, the produced T_L is expected to be smaller than that for for $\lambda_L = 2.5\,\mu$m. This argument in conjunction with the enhanced impact ionization for $\lambda_L = 2.5\,\mu$m can be used to explain the higher maximum lattice temperatures for $\lambda_L = 2.5\,\mu$m than for $\lambda_L = 2.2\,\mu$m, which in turn accounts for the predicted larger threshold for $\lambda_L = 2.2\,\mu$m [Fig. 8(a)]. In contrast, the above argument does not vary the order of the magnitudes of $\lambda_L = 3.3$ and $\lambda_L = 2.5\,\mu$m [Fig. 8(a)] as the three-photon absorption process for the latter wavelength is always stronger. This is also reflected on the impact ionization contribution to the excited carrier densities [59].

Certainly, it has to be noted that the aforementioned predictions require validation of the model with experimental results. The results illustrated in Fig. 9 indicate a good agreement of the theoretical calculations with the experimentally measured damage threshold values [64,71] for $\lambda_L = 3\,\mu$m at $\tau_p = 90$ fs. The relatively smaller damage thresholds for p-polarized beams compared to s beams are due to the larger

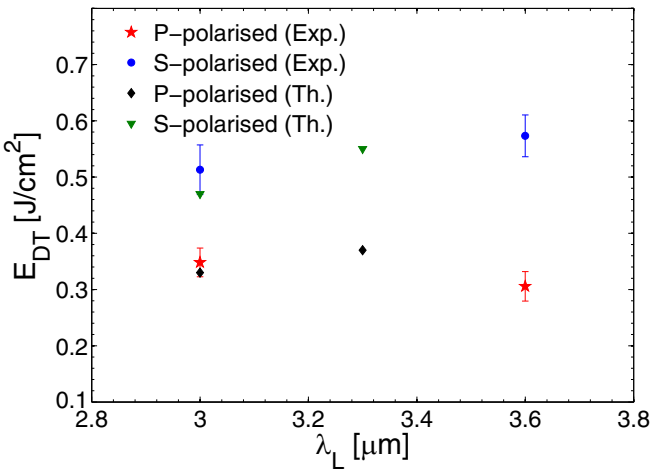

FIG. 9. Theoretical predictions of damage thresholds against experimental results for *s*- and *p*-polarized beams [64,71] ($\tau_p = 90$ fs, at 45° incident angle).

energy absorption for that polarization state. In contrast, for $\lambda_L = 3.6\,\mu$m at $\tau_p = 90$ fs, the experimental results are not compared with any simulated data as for this wavelength $\gamma_{\mathrm{TPA}} = 0$ [55], which suggests an appropriate revision of the model is required to take into account a four-photon absorption mechanism. This is beyond the scope of this work as the model aims to explore the spectral region in which two- and/or three-photon absorption mechanisms dictate the carrier excitation. Nevertheless, as a guide for the eye, simulated results for $\lambda_L = 3.3\,\mu$m at $\tau_p = 90$ fs are presented in Fig. 9. All data and simulations in Fig. 9 correspond to irradiation of the solid at a 45° angle of incidence (the evaluation of the reflectivity of the material was computed with mathematical expressions presented in Ref. [59]).

It is evident that a more accurate conclusion about the validity of the model will be drawn if more appropriately developed (for example, time-resolved) experimental protocols are introduced to evaluate the damage thresholds at the onset of the phase transition. To the best of our knowledge, there is not a sufficient number of similar reports with experimental results for the frequency range explored in this study. Furthermore, a more systematic experimental investigation and protocols will allow one to further test the accuracy of the parameter values in the model (for example, collision frequencies, effective masses, carrier-phonon relaxation time, influence of degeneracy) for mid-IR laser pulses.

There are also some yet unexplored issues that need to be addressed (i.e., excitation in very short pulses, structural effects in extreme conditions, more accurate behavior in ablation conditions, formation of voids inside the material after repetitive irradiation, role of incubation effects, etc.) before a complete picture of the physical processes that characterize heating of silicon with femtosecond mid-IR laser pulses is attained. Nevertheless, the methodology presented in this work aimed to provide an insight into the fundamental mechanisms in this area. Apart from the importance of elucidating the underlying mechanisms from a physical point of view, a deeper understanding of the thermal response of the material as well as the characteristics of electrodynamic effects (i.e., lifetime and extinction length of SP) will allow a systematic novel surface engineering with strong mid-IR fields.

IV. CONCLUSIONS

A detailed theoretical framework was presented that describes both the ultrafast dynamics and thermal response following irradiation of silicon with ultrashort pulsed lasers in the mid-IR range. Results demonstrated that the Kerr effect is important at lower wavelengths ($\sim 2.2\,\mu$m) and it leads to substantially large deviations to the maximum lattice temperature reached that affects the damage threshold. Furthermore, it is shown that although the heated material is initially transparent, during the duration of the pulse, the energy is confined in a less than ~ 100 nm depth.

A systematic analysis of the SP dispersion relation for mid-IR and comparison with results upon excitation with $\lambda_L = 800$ nm revealed that irradiation in the mid-IR region yielded SP that are weakly confined on the surface, exhibit longer lifetimes, and propagate on larger areas. These features can be potentially exploited to promote mid-IR-based technology to produce sensors and detectors or to present new capabilities in laser-based manufacturing.

Finally, theoretical predictions also revealed a $\tau_p^{\zeta(\lambda_L)}$ [$\zeta(\lambda_L) \sim 0.55$] dependence of the damage threshold for $\tau_p > 100$ fs. Moreover, analysis for $\lambda_L = 2.2\,\mu$m conclusively manifests the enhanced role of the impact ionization contribution at longer pulse durations, which eventually yield to a lower damage threshold for irradiation with laser pulses of $\lambda_L = 2.5\,\mu$m. Predictions resulting from the above theoretical approach demonstrate that unravelling phenomena in the interaction of matter with mid-IR pulses can potentially set the basis for the development of new tools for nonlinear optics and photonics for a large range of applications.

ACKNOWLEDGMENTS

The authors acknowledge financial support from Nanoscience Foundries and Fine Analysis (NFFA)–Europe H2020-INFRAIA-2014-2015 (Grant Agreement No. 654360), MouldTex project-H2020-EU.2.1.5.1 (Grant Agreement No. 768705), and COST Action TUMIEE (supported by COST-European Cooperation in Science and Technology).

[1] A. Y. Vorobyev and C. Guo, Laser Photon. Rev. **7**, 385 (2012).

[2] V. Zorba, L. Persano, D. Pisignano, A. Athanassiou, E. Stratakis, R. Cingolani, P. Tzanetakis, and C. Fotakis, Nanotechnology **17**, 3234 (2006).

[3] V. Zorba, E. Stratakis, M. Barberoglou, E. Spanakis, P. Tzanetakis, S. H. Anastasiadis, and C. Fotakis, Adv. Mater. **20**, 4049 (2008).

[4] D. Bäuerle, *Laser Processing and Chemistry*, 3rd ed. (Springer, Berlin, 2000).

[5] J.-C. Diels and W. Rudolph, *Ultrashort Laser Pulse Phenomena: Fundamentals, Techniques, and Applications on a Femtosecond Time Scale*, 2nd ed. (Elsevier/Academic, Amsterdam, 2006).

[6] E. L. Papadopoulou, A. Samara, M. Barberoglou, A. Manousaki, S. N. Pagakis, E. Anastasiadou, C. Fotakis, and E. Stratakis, Tissue Eng. Part C-Methods **16**, 497 (2010).

[7] Z. B. Wang, M. H. Hong, Y. F. Lu, D. J. Wu, B. Lan, and T. C. Chong, J. Appl. Phys. **93**, 6375 (2003).

[8] S. M. Petrovic, B. Gakovic, D. Perusko, E. Stratakis, I. Bogdanovic-Radovic, M. Cekada, C. Fotakis, and B. Jelenkovic, J. Appl. Phys. **114**, 233108 (2013).

[9] C. Simitzi, P. Efstathopoulos, A. Kourgiantaki, A. Ranella, I. Charalampopoulos, C. Fotakis, I. Athanassakis, E. Stratakis, and A. Gravanis, Biomaterials **67**, 115 (2015).

[10] M. Konstantaki, P. Childs, M. Sozzi, and S. Pissadakis, Laser Photon. Rev. **7**, 439 (2013).

[11] E. Stratakis, A. Ranella, and C. Fotakis, Biomicrofluidics **5**, 013411 (2011).

[12] J. Bonse, M. Munz, and H. Sturm, J. Appl. Phys. **97**, 013538 (2005).

[13] M. Huang, F. L. Zhao, Y. Cheng, N. S. Xu, and Z. Z. Xu, ACS Nano **3**, 4062 (2009).

[14] Zhou Guosheng, P. M. Fauchet, and A. E. Siegman, Phys. Rev. B **26**, 5366 (1982).

[15] G. D. Tsibidis, M. Barberoglou, P. A. Loukakos, E. Stratakis, and C. Fotakis, Phys. Rev. B **86**, 115316 (2012).

[16] G. D. Tsibidis, E. Skoulas, A. Papadopoulos, and E. Stratakis, Phys. Rev. B **94**, 081305(R) (2016).

[17] G. D. Tsibidis, E. Stratakis, and K. E. Aifantis, J. Appl. Phys. **112**, 089901 (2012).

[18] A. Papadopoulos, E. Skoulas, G. D. Tsibidis, and E. Stratakis, Appl. Phys. A **124**, 146 (2018).

[19] G. D. Tsibidis and E. Stratakis, J. Appl. Phys. **121**, 163106 (2017).

[20] G. D. Tsibidis, A. Mimidis, E. Skoulas, S. V. Kirner, J. Krüger, J. Bonse, and E. Stratakis, Appl. Phys. A **124**, 27 (2017).

[21] M. Birnbaum, J. Appl. Phys. **36**, 3688 (1965).

[22] J. Bonse, S. Höhm, S. V. Kirner, A. Rosenfeld, and J. Krüger, IEEE J. Sel. Top. Quantum Electron. **23**, 9000615 (2017).

[23] Y. Shimotsuma, P. G. Kazansky, J. R. Qiu, and K. Hirao, Phys. Rev. Lett. **91**, 247405 (2003).

[24] G. D. Tsibidis, C. Fotakis, and E. Stratakis, Phys. Rev. B **92**, 041405(R) (2015).

[25] J. E. Sipe, J. F. Young, J. S. Preston, and H. M. van Driel, Phys. Rev. B **27**, 1141 (1983).

[26] M. Barberoglou, G. D. Tsibidis, D. Gray, E. Magoulakis, C. Fotakis, E. Stratakis, and P. A. Loukakos, Appl. Phys. A: Mater. Sci. Proc. **113**, 273 (2013).

[27] G. D. Tsibidis, E. Stratakis, P. A. Loukakos, and C. Fotakis, Appl. Phys. A **114**, 57 (2014).

[28] J. JJ Nivas, S. He, A. Rubano, A. Vecchione, D. Paparo, L. Marrucci, R. Bruzzese, and S. Amoruso, Sci. Rep. Uk **5**, 17929 (2015).

[29] A. Margiolakis, G. D. Tsibidis, K. M. Dani, and G. P. Tsironis, Phys. Rev. B **98**, 224103 (2018).

[30] T. J. Y. Derrien, T. E. Itina, R. Torres, T. Sarnet, and M. Sentis, J. Appl. Phys. **114**, 083104 (2013).

[31] O. Varlamova, F. Costache, M. Ratzke, and J. Reif, Appl. Surf. Sci. **253**, 7932 (2007).

[32] D. R. Austin *et al.*, J. Appl. Phys. **120**, 143103 (2016).

[33] D. R. Austin *et al.*, Opt. Express **23**, 19522 (2015).

[34] R. Stanley, Nat. Photon. **6**, 409 (2012).

[35] A. D. Bristow, N. Rotenberg, and H. M. van Driel, Appl. Phys. Lett. **90**, 191104 (2007).

[36] F. Gholami, S. Zlatanovic, A. Simic, L. Liu, D. Borlaug, N. Alic, M. P. Nezhad, Y. Fainman, and S. Radic, Appl. Phys. Lett. **99**, 081102 (2011).

[37] B. Jalali, Nat. Photon. **4**, 506 (2010).

[38] A. Boltasseva and H. A. Atwater, Science **331**, 290 (2011).

[39] R. Soref, Nat. Photonics **4**, 495 (2010).

[40] H. M. van Driel, Phys. Rev. B **35**, 8166 (1987).

[41] S. K. Sundaram and E. Mazur, Nat. Mater. **1**, 217 (2002).

[42] T. J. Y. Derrien, J. Kruger, T. E. Itina, S. Hohm, A. Rosenfeld, and J. Bonse, Appl. Phys. A **117**, 77 (2014).

[43] E. Knoesel, A. Hotzel, and M. Wolf, Phys. Rev. B **57**, 12812 (1998).

[44] D. S. Ivanov and L. V. Zhigilei, Phys. Rev. B **68**, 064114 (2003).

[45] Z. Lin, L. V. Zhigilei, and V. Celli, Phys. Rev. B **77**, 075133 (2008).

[46] A. Rudenko, J.-P. Colombier, and T. E. Itina, Phys. Rev. B **93**, 075427 (2016).

[47] T. J. Y. Derrien, J. Krüger, and J. Bonse, J. Opt. **18**, 115007 (2016).

[48] H. Raether, *Surface Plasmons on Smooth and Rough Surfaces and on Gratings*, Springer Tracts in Modern Physics (Springer-Verlag, Berlin, 1988), Vol. 111.

[49] N. K. Hon, R. Soref, and B. Jalali, J. Appl. Phys. **110**, 011301 (2011).

[50] J. K. Chen, D. Y. Tzou, and J. E. Beraun, Int. J. Heat. Mass Transfer **48**, 501 (2005).

[51] A. Rämer, O. Osmani, and B. Rethfeld, J. Appl. Phys. **116**, 053508 (2014).

[52] S. I. Anisimov, B. L. Kapeliovich, and T. L. Perel'man, Zh. Eksp. Teor. Fiz. **66**, 776 (1974) [Sov. Phys. JETP **39**, 375 (1974)].

[53] K. Sokolowski-Tinten and D. von der Linde, Phys. Rev. B **61**, 2643 (2000).

[54] Q. Lin, J. Zhang, G. Piredda, R. W. Boyd, P. M. Fauchet, and G. P. Agrawal, Appl. Phys. Lett. **91**, 021111 (2007).

[55] S. Pearl, N. Rotenberg, and H. M. van Driel, Appl. Phys. Lett. **93**, 131102 (2008).

[56] D. Agassi, J. Appl. Phys. **55**, 4376 (1984).

[57] D. Chandler-Horowitz and P. M. Amirtharaj, J. Appl. Phys. **97**, 123526 (2005).

[58] C. D. Salzberg and J. J. Villa, J. Opt. Soc. Am. **47**, 244 (1957).

[59] See Supplemental Material at http://link.aps.org/supplemental/10.1103/PhysRevB.99.195201 for a detailed description of (i) maximum carrier dependence on the pulse duration, (ii) temporal variation of the impact ionization rate, (iii) carrier density as a function of the laser fluence, (iv) calculation of reflectivity for *s*- and *p*-polarized beams at an incident angle φ, (v) numerical simulation details, (vi) surface plasmon excitation conditions, and (vi) table of thermophysical and optical properties of Si.

[60] J. S. Preston and H. M. van Driel, Phys. Rev. B **30**, 1950 (1984).

[61] J. Bonse, A. Rosenfeld, and J. Krüger, J. Appl. Phys. **106**, 104910 (2009).

[62] D. Dufft, A. Rosenfeld, S. K. Das, R. Grunwald, and J. Bonse, J. Appl. Phys. **105**, 034908 (2009).

[63] R. M. Osgood, N. C. Panoiu, J. I. Dadap, X. P. Liu, X. G. Chen, I. W. Hsieh, E. Dulkeith, W. M. J. Green, and Y. A. Vlasov, Adv. Opt. Photon. **1**, 162 (2009).

[64] E. Chowdhury *et al.*, *Ultra-fast Bandgap Photonics in Mid-IR Wavelengths* (SPIE, Baltimore, Maryland, 2016), Vol. 9835, p. 983519.

[65] J. M. Pitarke, V. M. Silkin, E. V. Chulkov, and P. M. Echenique, Rep. Prog. Phys. **70**, 1 (2007).

[66] C. S. R. Nathala, A. Ajami, W. Husinsky, B. Farooq, S. I. Kudryashov, A. Daskalova, I. Bliznakova, and A. Assion, Appl. Phys. A **122**, 107 (2016).

[67] J. R. Meyer, M. R. Kruer, and F. J. Bartoli, J. Appl. Phys. **51**, 5513 (1980).

[68] D. P. Korfiatis, K. A. T. Thoma, and J. C. Vardaxoglou, J. Phys. D: Appl. Phys. **40**, 6803 (2007).

[69] J. Bonse, S. Baudach, J. Kruger, W. Kautek, and M. Lenzner, Appl. Phys. A **74**, 19 (2002).

[70] P. P. Pronko, P. A. VanRompay, C. Horvath, F. Loesel, T. Juhasz, X. Liu, and G. Mourou, Phys. Rev. B **58**, 2387 (1998).

[71] D. Austin, K. Kafka, C. I. Blaga, L. F. Dimauro, and E. Chowdhury, *Measurement of Femtosecond Laser Damage Thresholds at Mid-IR Wavelengths* (SPIE, Boulder, Colorado, 2014), Vol. 9237, p. 92370V.